REVIEWS OF TOPICAL PROBLEMS

**55th ANNIVERSARY OF THE INSTITUTE OF SPECTROSCOPY
OF THE RUSSIAN ACADEMY OF SCIENCES (ISAN)**

Experiments with nonlinear topological edge states in static and dynamically modulated Su–Schrieffer–Heeger arrays

Y V Kartashov, S K Ivanov, Y Q Zhang, S A Zhuravitskii, N N Skryabin, I V Dyakonov, A A Kalinkin, S P Kulik, V O Kompanets, S V Chekalin, V N Zadkov

Contents

Abstract. Progress in observation of solitons in photonic topological insulators is discussed. Results are presented of experiments with nonlinear topological states in Su–Schrieffer–Heeger arrays — fabricated using the femtosecond writing technique — that are static, i.e., invariable in the direction of light propagation, and dynamically modulated (primarily periodically) in the direction of light propagation. Such objects are one of the simplest models of a topologically nontrivial structure. Solitons in topological insulators bifurcate with increasing laser beam power from linear edge states in the topological bandgap, inheriting their topological protection. The spatial localization of the soliton and the position of its propagation constant in the topological bandgap depend in a nonlinear medium on peak power and can be effectively controlled. Experimental observation of the switching of the edge topological modes in the bandgap between two closely spaced dimerized Su–Schrieffer–Heeger arrays is presented. The switching, whose rate depends on radiation intensity, can be completely arrested in a strongly nonlinear regime. In trimer waveguide arrays, whose spectrum in the topological phase features two simultaneously emerging topological bandgaps with edge states of different symmetries, two coexisting types of topological solitons exhibiting different degrees of stability were observed. We also discuss experimental observations of π-solitons — nonlinear topological Floquet states periodically reproducing their profiles in 1D- and 2D-dimensional Su–Schrieffer–Heeger arrays modulated in the direction of propagation of radiation.

Keywords: Su–Schrieffer–Heeger arrays, topological solitons, switching, topological photonics

Y V Kartashov [(1,*)], **S K Ivanov** [(1)], **Y Q Zhang** [(2)], **S A Zhuravitskii** [(3)],
N N Skryabin [(3)], **I V Dyakonov** [(3)], **A A Kalinkin** [(3)], **S P Kulik** [(3)],
V O Kompanets [(1)], **S V Chekalin** [(1)], **V N Zadkov** [(1,4)]

[(1)] Institute of Spectroscopy, Russian Academy of Sciences,
   ul. Fizicheskaya 5, 108840 Troitsk, Moscow, Russian Federation
[(2)] Key Laboratory for Physical Electronics and Devices of the Ministry
   of Education & Shaanxi Key Lab
   of Information Photonic Technique, School of Electronic
   and Information Engineering, Xi'an Jiaotong University,
   710049 Xi'an, China
[(3)] Lomonosov Moscow State University, Quantum Technology Centre,
   Leninskie gory 1, str. 35, 119991 Moscow, Russian Federation
[(4)] National Research University Higher School of Economics
   (HSE University),
   ul. Myasnitskaya 20, 101000 Moscow, Russian Federation
E-mail: [(*)] kartashov@isan.troitsk.ru

1. Introduction

Topological insulators, which play an important role in physics, have been experimentally observed in a wide variety of physical systems. Interest in them is mainly due to the unusual propagation scenarios of excitations observed in such structures and the exceptional stability of unique topological edge states that arise at the interface between two materials described by Hamiltonians with different topological properties characterized by different integer topological invariants. In topological insulators, edge excitations that arise in the topological band gap in the spectrum are protected by the topology of the system itself and can propagate along the boundary of the structure, following all its bends and local deformations and overcoming localized defects without scattering, while behaving in the bulk like in a conventional insulator due to the presence of an energy band gap. Thus, perturbations with an amplitude that is not sufficient to close the topological band gap in the energy spectrum cannot lead to the destruction of edge states. Topological insulators were first predicted in solid-state physics, where it was discovered that the band structures of dielectric materials allow classification based on the topology of the space characterizing the electron states in the Brillouin zone. It was also found that the topological properties of the

bands can be described using an integer topological index (invariant) that does not change when perturbations are introduced into the Hamiltonian of the system, provided that such perturbations do not lead to the closure of the band gap in the energy spectrum (i.e., to the crossing of energy levels). Since a change in the topological indices of the bands is only possible when energy levels cross, intermediate edge states localized in the direction perpendicular to the boundary should arise at the interface between two materials with different band structure topologies, which can 'connect' bands with different values of the topological invariant in the spectrum of the system. The classification of band structures and the type of topological invariant describing the system are usually determined by the symmetry types of the corresponding Hamiltonian in k-space. An immense contribution to the study of such structures was made by Soviet researchers (see, for example, pioneering study [1], where topological surface states in 3D topological insulators were predicted and recent reviews published in Russian [2–4] and foreign [5, 6] journals). Over the past ten years, the concept of topological insulators has expanded significantly, and similar structures have been observed in experiments involving mechanical systems [7, 8], acoustics [9–11], atomic systems in optical lattices [12–16], exciton-polariton condensates in structured microresonators [17–24], and optical [25–31] and many other systems. Recent advances in topological photonics, where topological insulators, in addition to the interest in their purely fundamental physics, can also find many practical applications, are described in reviews [32–35].

In solid-state physics, nontrivial topological properties of a material are determined by the band structure of its spectrum, i.e., by the structure of the material itself, as has been shown in such materials or heterostructures as PbTe/SnTe and HgTe/CdTe [1–6]. In optics, the band structure topology can be controlled by modulating the refractive index of the medium. Optical topological insulators, like their analogs in solid-state physics, feature a complete band gap in the spectrum, i.e., excitations with certain frequencies cannot propagate in the bulk of such materials, but, at the same time, they support propagating edge states at frequencies belonging to the band gap at their interface with a material with a different topology. Topological insulators, experimentally demonstrated at optical frequencies, can be conditionally divided into several large groups.

The first one among them includes insulators with broken 'time'-reversal symmetry (in optics, the role similar to time can be played by the coordinate of optical radiation propagation). One of the simplest ways to break this symmetry is to use gyromagnetic materials in external magnetic fields [25], but, since the band gap (and, consequently, the degree of protection of edge states) that can be achieved in such materials at optical frequencies is small, experiments with such structures have been carried out primarily in the microwave range. The above-mentioned symmetry can be violated using helical waveguides [28], which made it possible to observe unidirectional edge states in honeycomb arrays of waveguides. Square lattices of periodically approaching waveguides also enabled observation of anomalous topological phases [29, 30], when edge states arise due to longitudinal modulation of the refractive index. In fact, the above-mentioned systems also belong to the class of Floquet insulators [36–38], in the sense that the usual band structure of the spectrum is replaced in them by a Floquet spectrum for quasi-energies, which is periodic not only with respect to the Bloch momentum but also along the quasi-energy axis.

Another broad class of optical topological insulators consists of structures based on the valley Hall effect: they are waveguide systems or photonic crystals in which two lattices consisting of sublattices with different detunings/deformations that violate the inversion symmetry of the system form a domain wall, where topological edge modes appear [39–43]. These insulators, however, are characterized by the coexistence of edge states on one domain wall, propagating in two different directions, and sufficiently narrow defects on the domain wall can lead to the binding of such states. Therefore, it is generally accepted that optical structures based on the valley Hall effect are characterized by weaker topological protection of edge states.

Finally, it is worth separately distinguishing a wide class of higher-order insulators [44–47]. Having a dimension of D, they feature $(D-1)$-dimensional boundaries that do not support unidirectional states, but are themselves topological insulators. A D-dimensional topological insulator of the Nth order is characterized by the presence of edge states localized on its $(D-N)$-dimensional boundary. For such structures, the correspondence principle, which relates the number of edge states arising at the boundary to the standard topological invariants of the band structure of a periodic material, is not applicable in its usual form.

Until recently, topological insulators had been studied exclusively in the linear regime. However, an unquestionable advantage of optical topological structures is that the materials from which they are created often feature a fairly strong nonlinear response. It turns out that in the nonlinear regime the propagation dynamics and the conditions for the emergence of edge states can alter qualitatively [48–50], and nonlinearity allows a controlled rearrangement of the energies of edge states in the band gap, thereby changing their spatial localization [51]. Nonlinearity can be used to implement effective parametric interactions of edge states and generate new harmonics, which themselves can be localized near the boundary of the structure [52–54]. It is worth noting that the nonlinearity of the medium can even lead to the emergence of self-induced topological phases, when a system that is topologically trivial at low radiation intensity becomes nontrivial and begins supporting edge states at a quite high intensity [55–58]. Moreover, nonlinearity can lead to coupling of topological modes of different effective dimensions, such as corner and edge modes in higher-order insulators [59]. Nonlinearity can also initiate the development of modulation instability of edge states [16, 60, 61], leading to their splitting into a sequence of localized wave packets propagating along the topological structure boundary.

This phenomenon is a direct indication of the possible existence of solitons of a topological nature in topological insulators, recently predicted both in the bulk [62, 63] and at the boundary [64–75] of these structures. Such unique hybrid states, on the one hand, inherit the topological protection of the linear edge states from which they bifurcate, and, on the other hand, remain localized due to self-action in a nonlinear medium, including when propagating along the boundary of the insulator and interacting with its defects. Due to these features, they are of great interest for practical applications.

Edge solitons have been observed experimentally in various topological optical systems, including Floquet insulators [71, 72] and higher-order insulators [76, 77]. The theory

of envelope solitons, based on topological edge states that hardly radiate during propagation, has been developed for both discrete [64–66] and continuous [68–70] models describing systems with helical waveguides. Edge solitons have also been found in optical systems based on the valley Hall effect [73–75]; they have been observed not only in as-fabricated structures but also in tunable optical lattices induced in hot atomic vapors [67]. The theory of topological solitons in aperiodic structures such as arrays with disclinations is currently being actively developed [78, 79].

One of the most challenging problems in the theory of nonlinear topological optical insulators is the topological description of nonlinear systems and the issue of the applicability of topological invariants for predicting the occurrence of edge states in a system when a nonlinear addition to the refractive index significantly alters the distribution of its refractive index. A preliminary analysis [76] of higher-order insulators showed that, even in this case, when taking into account the nonlinear deformation of the refractive index profile, a topological invariant can be introduced equivalent to conventional bulk polarization, which correctly predicts the formation of corner modes in the system. Further potential progress in this area may be associated with the introduction of invariants based on the Green's function of the system, developed in the theory of interacting topological systems in solid-state physics [80–82].

An example of the simplest topological structure in which topological solitons can form is the Su–Schrieffer–Heeger lattice [83], where a transition to the topological phase is realized due to shifts of individual sites in the dimers of which the structure consists. In this phase, edge states arise at the lattice boundary, from which, in the presence of nonlinearity, edge solitons bifurcate, which have been found theoretically [84–89] and, in a weakly nonlinear regime, observed experimentally in waveguide structures [90–92], optical fibers [93], and structured polariton microresonators [94, 95]. Most of the experiments with weakly nonlinear edge states and edge solitons were performed in Su–Schrieffer–Heeger lattices with one topological band gap, allowing the formation of edge solitons of only one type. The coexistence of several edge solitons with different internal structures requires the introduction of more complex topological structures consisting of trimers or quadrimers of waveguides, as predicted in [96–100] and only recently confirmed experimentally in our study [101]. Su–Schrieffer–Heeger linear arrays can also be used to construct fairly complex 2D structures, for example, a star-shaped configuration, in which defect and several types of topological solitons can simultaneously coexist [102].

Interestingly, when constructing one-dimensional Su–Schrieffer–Heeger topological lattices, the same approach is used as for constructing higher-order insulators, when a shift of sites (in our case, waveguides) in a unit cell containing two sites a and b changes the coupling strength (which determines the tunneling rate of the light field energy) between sites inside the cell and between sites in neighboring cells. Thus, in the approximation of strongly localized modes (i.e., in the one-dimensional discrete model), which takes into account only the coupling between neighboring lattice sites, the lattice Hamiltonian takes the form $\mathcal{H} = -\sum_n [t_1 | n, b\rangle\langle n, a| + t_2 | n + 1, a\rangle\langle n, b|] + \text{h.c.}$, where n is the number of the current cell, t_1 is the constant of coupling between sites within the unit cell, and t_2 is the constant of coupling between adjacent sites from different cells. When switching to the quasi-momentum

k-space, we represent the state vectors in the form $|n, x\rangle = N^{-1/2} \sum_k \exp{(\mathrm{i}kn)} |k, x\rangle$, where $k \in [-\pi, \pi)$ is the Bloch momentum, N is the total number of cells in the structure, and $x = a, b$ denotes the type of lattice site. Then, the lattice Hamiltonian can be represented as $\mathcal{H} = \sum_k \mathcal{H}_k |k\rangle\langle k|$, where

$$\mathcal{H}_k = \begin{pmatrix} 0 & -t_1 - t_2 \exp{(-\mathrm{i}k)} \\ -t_1 - t_2 \exp{(+\mathrm{i}k)} & 0 \end{pmatrix}.$$

A topologically nontrivial phase, in which edge states arise at the boundary of a truncated lattice, is realized when $t_1 < t_2$, i.e., when the constant of coupling between sites in neighboring cells exceeds that between sites in a cell. It should be emphasized that in such a discrete description the system is characterized by symmetry with respect to time reversal $\mathcal{T}\mathcal{H}_k\mathcal{T}^{-1} = \mathcal{H}_{-k}$, chiral $\sigma_z\mathcal{H}_k\sigma_z = -\mathcal{H}_k$, and inversion $\sigma_x\mathcal{H}_k\sigma_x = \mathcal{H}_{-k}$ symmetries, and particle-hole symmetry $\mathcal{C}\mathcal{H}_k\mathcal{C}^{-1} = -\mathcal{H}_{-k}$, where $\mathcal{C} = \sigma_z\mathcal{T}$, σ_x, σ_z are the Pauli matrices. The presence of these symmetries enables us to classify this structure as a class of topological systems described by the $\mathbb{Z}$ invariant ('the winding number' (see Section 3)).

Due to the topological protection of edge states, they are ideal candidates for implementing various disorder-tolerant switching and routing schemes and data or energy transmission [103–105]. The study of such systems and switching mechanisms involving edge states is of especial importance in optics, where these switches can be ultrafast. Various mechanisms for coupling between topological edge states have already been proposed. They include, in particular, topological pumping, in which energy is transferred from one insulator boundary to another as a result of an adiabatic change in the structure parameters [106, 107], the creation of an optical potential gradient along the insulator boundary, leading to periodic switching of excitations between opposite boundaries due to anomalous Bloch oscillations [108, 109], small longitudinal modulations of the optical potential, leading to Rabi oscillations between edge states [110, 111], the use of resonant pumping in microresonator systems, which allows selective excitation of modes at various structure boundaries [112, 113], and switching between closely spaced Floquet arrays with helical waveguides [114] or in small-sized Su–Schrieffer–Heeger chains [115, 116]. It is only recently that we have experimentally presented the use of nonlinearity of optical material to control the dynamics of such switching between edge states in Su–Schrieffer–Heeger arrays [117].

Optical systems, in which topologically nontrivial phases arise due to periodic modulations of the refractive index of the structure in the direction of radiation propagation, provide new options for controlling the propagation dynamics [118]. The topological classification of such systems requires introducing specially defined invariants, as shown in [119–121]. Modulated Su–Schrieffer–Heeger arrays are one of the simplest examples of such structures supporting anomalous π-modes, the existence of which is associated with the topological π-invariant for Floquet systems [122–127]. These modes arise even in structures that spend half of the longitudinal period in the topologically trivial phase and are topologically nontrivial only in the other half of the period. In the Floquet system spectrum, these modes usually appear between Floquet replicas of the same allowed band, arising due to the longitudinal modulation of the refractive index.

Previously, π-modes were observed only in the linear regime in 1D modulated Su–Schrieffer–Heeger lattices in the microwave range [128] and at optical frequencies in non-Hermitian or plasmonic lattices [129–131] with a high refractive index contrast, where, however, significant losses limit the propagation range of edge states to hundreds of micrometers. π-modes were also observed in acoustics [132, 133]. In the presence of nonlinearity, π-modes in the Floquet system make it possible to obtain a family of π-solitons bifurcating from them: unique nonlinear topological states that exactly reproduce their profile after each longitudinal modulation period [134, 135]. Such 1D and 2D nonlinear states have been experimentally observed only recently in oscillating waveguide arrays [136].

The above results indicate that even the simplest topological systems based on Su–Schrieffer–Heeger lattices allow observing some unique physical phenomena and topological states arising due to the interaction of the nontrivial topology of the system and self-action effects. In this review, we present a brief description of the experiments and results obtained at the Institute of Spectroscopy of the Russian Academy of Sciences on static and dynamically modulated 1D and 2D Su–Schrieffer–Heeger lattices in essentially nonlinear propagation regimes, when a nonlinear addition to the refractive index becomes comparable to the modulation depth of the refractive index in the topological structure itself. In particular, in Section 2, we discuss the observation of nonlinearity-controlled switching between the edge states of two closely located dimerized Su–Schrieffer–Heeger topological arrays. When two such arrays approach each other, the overlap of the wave fields of the topological states results in their periodic switching between the arrays, the switching rate being dependent on the input beam intensity and the distance between the arrays [117]. It is of importance to note that, unlike conventional splitters [137, 138], in our system switching occurs between states from the topological band gap, the localization of which directly depends on the band gap width. An increase in nonlinearity first leads to suppression of switching and then can cause a sharp increase in radiation into the bulk of the arrays. In Section 3, we present the observation of topological solitons in a trimer array whose spectrum contains two topological band gaps, where edge states with different internal structures and symmetries exist [101]. Edge solitons bifurcating from such edge states also feature different symmetries, one of the states being significantly more stable. Our experiments show that, unlike conventional surface solitons in nontopological lattices, topological solitons of both types can be excited even at low power. Finally, in Section 4, we consider the features of the spectrum of modulated Su–Schrieffer–Heeger lattices, which, due to the periodic variation in the coupling constant within and between the dimers of which the structure consists, spend half of the z-period in the 'instantaneous' topological phase, while in the other half of the period they are 'instantaneously' nontopological. Nevertheless, localized π-modes can arise at the boundaries of such arrays with π-solitons bifurcating from them in the nonlinear regime, which we observed in both 1D and 2D geometries [136].

2. Nonlinearity-controlled switching between topological states

One of the simplest and best-known models of a topological insulator is the Su–Schrieffer–Heeger model [83], which describes an array whose unit cell contains two sites (for example, two waveguides). Arrays of shallow (refractive index contrast $\delta n \sim 10^{-4}$) waveguides fabricated using the femtosecond laser writing technique provide a unique platform for implementing the Su–Schrieffer–Heeger model. In particular, to implement edge state switching between topologically nontrivial structures, we consider two closely spaced Su–Schrieffer–Heeger arrays [117]. The propagation of radiation in such a system in the paraxial approximation is described by the dimensionless Schrödinger equation for the light field amplitude ψ:

$$\mathrm{i}\frac{\partial\psi}{\partial z} = -\frac{1}{2}\left(\frac{\partial^2\psi}{\partial x^2} + \frac{\partial^2\psi}{\partial y^2}\right) - \mathcal{R}(x,y)\psi - |\psi|^2\psi. \qquad (1)$$

It should be noted that Eqn (1) can be represented as $\mathrm{i}\partial\psi/\partial z = \mathcal{H}\psi - |\psi|^2\psi$, where $\mathcal{H} = -(1/2)(\partial^2/\partial x^2 + \partial^2/\partial y^2) - \mathcal{R}$ is the Hamiltonian of the linear system. Here, the function $\mathcal{R}(x,y) = \mathcal{R}_{\mathrm{l}}(x,y) + \mathcal{R}_{\mathrm{r}}(x,y)$, where $\mathcal{R}_{\mathrm{l,r}}(x,y) = p\sum_{m=1,2N}\mathcal{Q}(x - x_{\mathrm{lm,rm}},y)$ describes the refractive index distribution in two 'linear' arrays written sufficiently close to each other, p is the normalized modulation depth of the refractive index in each of the arrays, and x_{lm}, x_{rm} are the coordinates of the waveguide centers in the left (subscript l) and right (subscript r) arrays. Each array consists of N pairs of waveguides with identical Gaussian profiles $\mathcal{Q}(x,y) = \exp[-(x^2 + y^2)/a^2]$ of width a. In dimensionless equation (1), the coordinates x, y are normalized to the characteristic transverse scale $r_0 = 10$ μm, the propagation coordinate z is normalized to the diffraction length kr_0^2, and the normalized modulation depth of refractive index $p = k^2 r_0^2 \delta n/n$ is proportional to the actual modulation depth of refractive index δn. Here, $k = 2\pi n/\lambda$ is the wave number in the medium, $n \approx 1.45$ is the unperturbed refractive index of the medium, (fused silica), and $\lambda = 800$ nm is the operating wavelength. The dimensionless intensity of the light field $|\psi|^2$ corresponds to the actual dimensional intensity $I = n|\psi|^2/k^2 r_0^2 n_2$, where the nonlinear refractive index for fused silica is $n_2 \approx 2.7 \times 10^{-20}$ m^2 W^{-1}. The typical width of the waveguides in such an array is $a = 0.5$ (about 5 μm). It should be noted that here and below we use the continuous model (1) to describe the propagation of radiation in Su–Schrieffer–Heeger lattices, which takes into account the actual refractive index profile in the medium and, as a consequence, the coupling between all waveguides in the structure, thereby providing a more complete description of the propagation dynamics compared to the simplified discrete model mentioned in the introduction. The continuous system (1) may lack some symmetries specific to the discrete model, although both models yield qualitatively similar linear spectra and band structure properties (although the discrete model, unlike the continuous one, describes only the two upper bands of the system). These differences are manifested in the linear spectrum, which, for example, in the continuous model is not completely symmetric with respect to the propagation constant of the edge state. System (1) is symmetric with respect to time reversal (propagation coordinate z), and also features inversion symmetry in the case of a single lattice.

Micrographs of a single Su–Schrieffer–Heeger array and a pair of such closely spaced structures are displayed in Fig. 1a. The arrays for these experiments are fabricated at the Quantum Technologies Center of Moscow State University by femtosecond laser writing in 10-cm fused silica slabs using
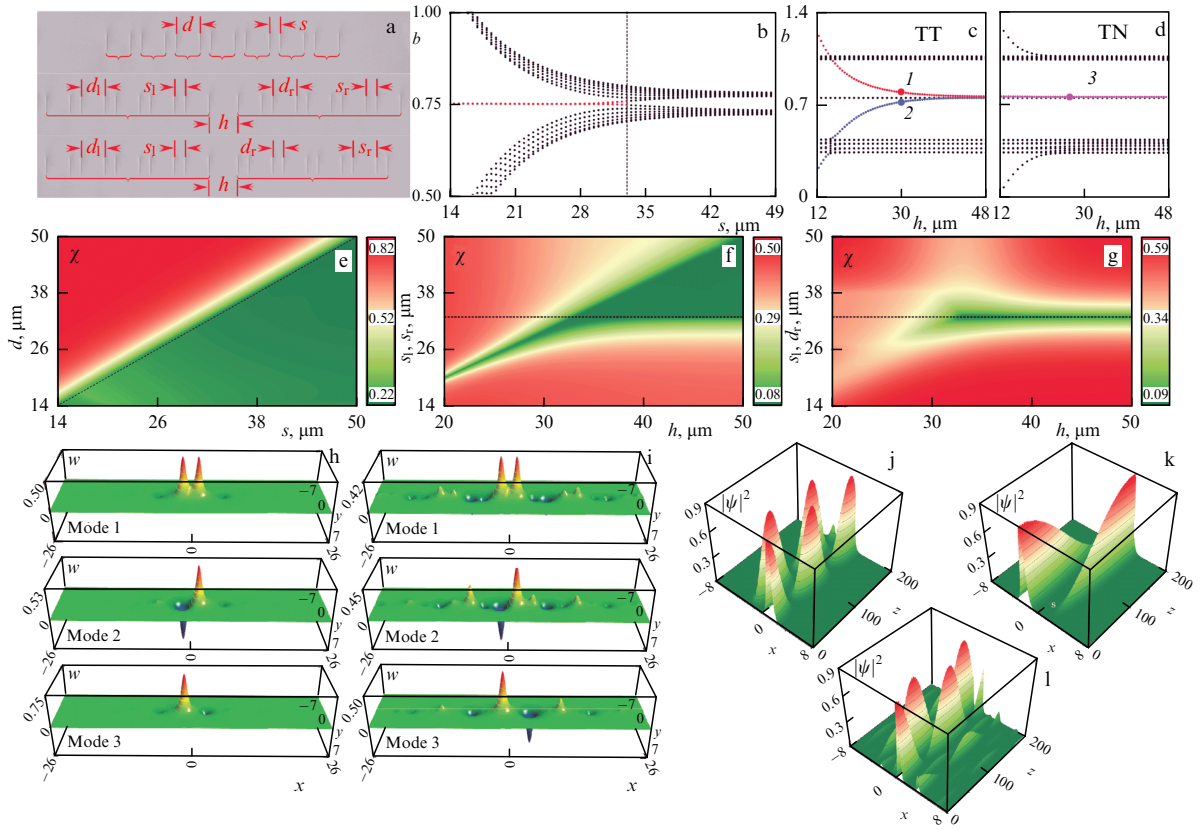
Figure 1. (a) Photomicrograph of a single Su–Schriffer–Heeger array fabricated by femtosecond laser writing in topological regime, where distance between waveguides in adjacent dimers $s = 15$ μm is smaller than distance $d = 33$ μm between waveguides inside dimers (top). Images of interface between two topological arrays with $s_l = s_r = 15$ μm and $d_l = d_r = 33$ μm (middle) and interface of a topological and a nontopological array with $s_l = d_r = 15$ μm and $s_r = d_l = 33$ μm (bottom). The two arrays are separated by distance h. (b) Linear spectrum of an array with 7 dimers as a function of distance s at a fixed $d = 33$ μm. Vertical dotted line denotes transition from nontopological phase to topological one at $s = d$. Eigenvalues of the modes supported by topological–topological ($s_l = s_r = 15$ μm, $d_l = d_r = 33$ μm) (c) and topological–nontopological ($s_l = d_r = 15$ μm, $s_r = d_l = 33$ μm) (d) arrays as a function of distance h between the two arrays. (e) Form factor of most localized linear mode in a single Su–Schrieffer–Heeger array as a function of distances s and d. Dotted line marks transition from nontopological phase (green region), in which edge states do not arise, to topological phase (red region), in which localized edge states appear at the array boundary. (f) Form factor of most localized linear mode at topological–topological array interface as a function of distance between arrays h and distance $s_l = s_r$ at a fixed $d_l = d_r = 33$ μm. Dotted horizontal line corresponds to $s_{l,r} = 33$ μm. (g) Form factor of most localized mode at boundary of topological–nontopological array as a function of h and $s_l = d_r$ for a fixed $s_r = d_l = 33$ μm. (h) Examples of profiles of $w(x, y)$ of strongly localized modes corresponding to points in panels (c) and (d). (i) Examples of profiles of $w(x, y)$ of weakly localized modes for the case of $s_l = s_r = 26$ μm, $d_l = d_r = 33$ μm (TT structure) and $s_l = d_r = 26$ μm, $s_r = d_l = 33$ μm (TN structure). Switching dynamics in TT structure for same set of parameters as in figure (h) for $h = 30$ μm (j) and $h = 40$ μm (k), and for the parameters from panel (i) for $h = 30$ μm (l). In all cases, normalized modulation depth of refractive index in the array is $p = 4.88$.

focused (via an aspherical lens with NA = 0.3) femtosecond laser pulses (at a wavelength of 515 nm, pulse duration of 280 fs, pulse energy of 360 nJ, and repetition rate of 1 MHz). In the process of writing, the sample is translated relative to the beam focus at a constant velocity of 1 mm s^{-1} using a high-precision positioning system (Aerotech), which allows fabrication of arrays of parallel waveguides with a controlled distance between them. A typical modulation depth of the refractive index in such arrays is $\delta n \sim 5.5 \times 10^{-4}$ (which corresponds to $p \sim 4-5$), i.e., these waveguides are single-mode ones with typical mode field diameters of $\sim 15.4 \times 24.0$ μm. Waveguides written in this way feature low losses, not exceeding 0.07 cm^{-1} at an operating wavelength of 800 nm.

In Su–Schrieffer–Heeger arrays, the topological phase is realized by means of an opposite shift of two waveguides in each unit cell (for zero shift, the array is a periodic structure with the same distance between all waveguides). A variation in the distance d between the waveguides in a cell (dimer) results in a change in the distance s between the waveguides in

adjacent cells, which is reflected in the coupling (arising from the overlap of the wave fields of the modes of two closely located waveguides) within each dimer and between dimers (see the notations in the micrograph of a single array presented in the upper row of Fig. 1a). When the coupling between dimers exceeds the bond inside the dimer, the structure passes into a topologically nontrivial phase, in which its truncation is accompanied by the appearance of edge states at its boundaries. The linear modes of the array can be found in the form $\psi(x, y, z) = w(x, y) \exp(ibz)$ (here, b is the mode propagation constant and $w(x, y)$ is a real function describing its profile). In the linear spectrum of a single array consisting of $N = 7$ dimers (shown in Fig. 1b), the propagation constants of the edge topological states in the topological band gap are indicated by red dots, while the black dots correspond to the delocalized bulk modes. The localization of the edge states increases with decreasing distance s between the dimers at a fixed $d = 33$ μm. The width of the topological band gap, where the edge states appear, also increases with decreasing distance s. At $s > d$, the

array passes into a trivial phase and, despite the presence of a band gap in its spectrum, the edge states no longer appear in it in this regime. This is also clearly seen from the dependence of the form factor $\chi = [U^{-2} \iint |\psi|^4 \, \mathrm{d}x \, \mathrm{d}y]^{1/2}$, where $U = \iint |\psi|^2 \, \mathrm{d}x \, \mathrm{d}y$ is the power calculated for the most localized linear mode in the Su–Schrieffer–Heeger array, on the distances s and d, displayed in Fig. 1e. It is noteworthy that the form factor of a mode is inversely proportional to its width, i.e., a more localized mode has a larger form factor, while weakly localized modes correspond to small values of χ. It is evident from this dependence that localized states at the boundary appear precisely at $s < d$, in the red region, while, in the green region, this array does not have localized modes (the form factor in the green region, where only delocalized bulk modes exist, decreases with increasing number of cells in the system, i.e., $\chi \to 0$ at $N \to \infty$). With an increasing number of dimers in the array, the density of delocalized states in the allowed band increases, but the propagation constants of the edge modes remain virtually unchanged. Generally speaking, the finite size of the system only manifests itself at $s \to d$, when the width of the edge modes becomes comparable to that of the array. In this case, the coupling of modes at opposite boundaries leads to the removal of the degeneracy of the propagation constants of the in-phase and out-of-phase combinations of edge states arising at opposite ends of the array (which is visible in a small region at $s > 30$ μm in Fig. 1b).

To observe the edge state switching, we created two closely spaced Su–Schrieffer–Heeger arrays, each consisting of $N = 5$ dimers. Micrographs of the two different configurations discussed below are shown in the middle and bottom rows of Fig. 1a, where the different arrays are highlighted by horizontal red brackets. In the first topological-topological (TT) configuration displayed in the middle row, both the left and right arrays are in the topological phase, since the spacing between dimers $s_l = s_r = 15$ μm (here, the subscript denotes the right or left array) in both arrays is smaller than the spacing between the waveguides inside dimers $d_l = d_r = 33$ μm. The bottom row of Fig. 1a displays the second, topological-nontopological (TN) configuration, in which the left array is in the topological phase, while the right one is in the trivial phase, which is achieved, for example, at $s_l = d_r = 15$ μm and $s_r = d_l = 33$ μm. The arrays are separated by a distance h, which varied in the experiments in a range from 15 to 46 μm.

To explain the mechanism of switching the edge states, we calculated the linear spectrum of the TT configuration as a function of the distance h between the two arrays (Fig. 1c). The spectrum clearly shows the topological band gap between the two bands, in which only bulk modes exist. The states corresponding to the red and blue lines in the band gap are the in-phase and out-of-phase modes formed at the interface of the two arrays (modes 1 and 2 in Fig. 1h). Their propagation constants vary depending on h. Two other modes, corresponding to black dots inside the band gap, whose propagation constants do not depend on h, are located at the outer edges of the arrays and not excited in the experiment. Figure 1f shows the dependence of the form factor of the most localized mode in the TT configuration on the distance h between the arrays and on the distance $s_l = s_r$ between the waveguides in adjacent dimers at a fixed distance between waveguides $d_l = d_r = 33$ μm inside the dimers. Here, at sufficiently large distances h, localized topological modes at the interface of two arrays also arise at $s_{l,r} < d_{l,r} = 33$ μm (lower red region).

It should be noted that defect localized modes can also arise in this system: such nontopological modes are associated with the upper red region in Fig. 1f. These modes are also visible in Fig. 1c — their propagation constants leave the topological band gap to the semi-infinite one when h changes.

Focusing the radiation into the waveguide at the interface between two arrays in the TT configuration is equivalent to the simultaneous excitation of the in-phase mode 1 and the out-of-phase mode 2 with nearly equal weights. The subsequent switching can be interpreted as periodic beats between these edge states, with the beat length inversely proportional to the difference in their propagation constants $L = \pi/(b_1 - b_2)$. Apparently, L increases with increasing distance h due to the decrease in the difference $b_1 - b_2$. Examples of the switching dynamics of topological edge states for various distances h between the arrays are shown in Figs 1j and 1k. Here, we consider arrays with sufficiently small distances $s_{l,r}$, which provides strong localization of the edge states and their efficient excitation in the experiment. However, it should be emphasized that switching is also possible for weakly localized edge states, even when $s_{l,r} \to d_{l,r}$. Examples of such edge states in the TT structure, which deeply penetrate into each of the arrays for the specified parameters, are presented in Fig. 1i. The switching dynamics for such weakly localized states is shown in Fig. 1l. In these states, particularly noticeable are the oscillating tails, where the field changes sign in neighboring dimers, typical of modes from the topological band gap.

When the topological and nontopological arrays approach each other (TN configuration), in the linear spectrum in the band gap, in addition to the modes at the outer boundaries, only one mode 3 appears, which is localized near the interface of two arrays (see the magenta dots in Fig. 1d), in the rightmost waveguide of the topological structure (see the profile in the last row of Fig. 1h,i), although it penetrates into the nontopological array. The form factor of the most localized mode as a function of the distance h between the arrays and the distance $s_l = d_r$ at fixed $s_r = d_l = 33$ μm for the TN structure is shown in Fig. 1g (note: to make one array topological and the other nontopological, here, we set the distance between dimers in one array equal to the distance between waveguides inside dimers in the other array). In such a configuration, one of the arrays is always in the topological state, except for the case $s_l = s_r$ ($d_l = d_r$), when all modes become delocalized. In the TN structure, focusing the beam into the topological (in our case, the left) part of the structure excites the localized mode 3, while focusing it into the right array should only lead to diffraction, since this part of the structure does not have localized states. In both cases, switching of edge states in the TN structure will not be observed.

For experimental observation of the switching of edge states, a set of TT and TN structures was fabricated for various distances h between the two arrays in the range from 15 to 46 μm. In the experiment, the light from a 1-kHz femtosecond Spitfire HP Ti:sapphire laser system (Spectra Physics), generating 40-fs pulses at a central wavelength of 800 nm, first passes through a system of active beam position stabilization (Avesta) and an attenuator, and then through a two-pass single-lattice compressor with a variable slit, which allows selecting a specific spectral region for optimizing the output pulse duration. The maximum nonlinear localization in our lattices is observed at a spectral width of ~ 5 nm and a pulse duration of $\tau \sim 300$ fs (FWHM). Such pulses were
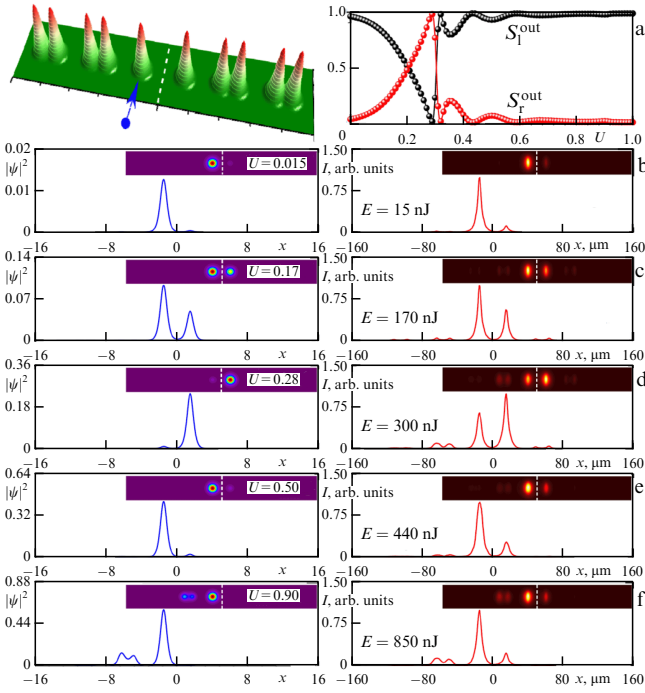
Figure 2. (a) Schematic representation of interface between two topological arrays with excited waveguide in left array indicated and calculated distribution of output power between left, S_l^{out}, and right, S_r^{out}, arrays as a function of input power U. (b–f) Comparison of calculated (blue lines) and experimentally measured (red lines) output intensity cross sections at $y = 0$ and 2D intensity distributions (insets) for increasing input pulse energies E. Vertical dashed lines in insets separate the two arrays. Here, $s_l = s_r = 15$ μm, $d_l = d_r = 33$ μm, $h = 30$ μm, and $p = 4.88$.

focused into a waveguide at the interface of the two arrays, as schematically shown by the blue arrow in the upper row of Figs 2–4. The temporal dynamics of the pulses over a sample length of 10 cm can be disregarded, while the spatial dynamics is accurately described by Eqn (1). Since the two arrays are equivalent in the TT structure, the outmost waveguide in the left array was excited. The output intensity distributions were recorded using Kiralux, a 12.3-megapixel scientific CMOS camera (Thorlabs). Taking into account losses on matching with the waveguide mode, the input peak power in the waveguide, which can be defined as the ratio of the pulse energy E to its duration τ, is estimated to be 2.5 kW per nanojoule.

The observation of the nonlinearity-controlled switching between the two topological arrays for $h = 30$ μm is presented in Fig. 2. The waveguide into which the laser light in the left array was focused is indicated by the blue arrow. For the chosen distance h, the sample length approximately corresponds to two beat lengths $2L$, i.e., in the linear regime, the light is first switched to the right array and then returned to the left one. To take into account the effect of nonlinearity, Fig. 2a shows the theoretically calculated fraction of the power concentrated at the output of a 10-cm sample in the left and right arrays

$$S_l^{out} = U^{-1} \int_{-\infty}^{0} dx \int_{-\infty}^{\infty} dy\, |\psi|^2 ,$$

$$S_r^{out} = U^{-1} \int_{0}^{\infty} dx \int_{-\infty}^{\infty} dy\, |\psi|^2 \qquad (2)$$

as a function of the input power

$$U = \int_{-\infty}^{\infty} dx \int_{-\infty}^{\infty} dy\, |\psi|^2 .$$

The nonlinearity slows down the switching, leading first to a concentration of light in the right array, and then completely suppresses it, so that at high powers the light always remains in the left array. Indeed, the nonlinearity changes the difference in the propagation constants of the in-phase and out-of-phase modes (since it affects them differently due to their different internal structure), which is manifested in a change in the interference pattern at the output of the sample with increasing power. The switching curves are fairly sharp; they are characterized by a rapid change in $S_{l,r}^{out}$ around $U \sim 0.3$. The right column of Fig. 2 shows the 1D experimental output intensity sections at $y = 0$ and the corresponding full 2D distributions for various pulse energies E. In the linear regime, $E = 15$ nJ, the light switches from the left array to the right one, and then returns to the left array. Increasing the pulse energy results in a gradual concentration of light in the right array, which is maximum at $E \sim 300$ nJ. It should be noted that, due to the pulsed nature of excitation for a given distance, some fraction of the radiation still remains at the left-array output. The reason is that, although the high-intensity parts of the pulse are switched to the right array, the low-intensity tails of the pulses are still switched linearly, contributing to the output power in the left array. With a further increase in the pulse energy to $E \sim 440$ nJ, the light is concentrated in the left array and remains there in a fairly wide energy range. Since in our system the switching occurs for edge states from the finite band gap, at a sufficiently high power the propagation constants of such states can shift to the allowed band (Fig. 1c), which leads to coupling with bulk modes and emission into the depth of the topological structure, clearly visible in Fig. 2f for $E \sim 850$ nJ. For comparison with the experimental data, the left column of Fig. 2 displays the theoretical intensity distributions obtained from Eqn (1) for single-channel excitation. It can be concluded that the main features of switching are reproduced well in theory. It should be emphasized that the observed switching is a stable phenomenon: fluctuations in the output power in the two arrays remain small at all input powers, and they are associated only with small fluctuations in the power in the input laser beam.

We also investigated the switching in a similar TT configuration, but with the distance between the two topological arrays increased to $h = 36$ μm (Fig. 3). In this case, the sample length corresponds to approximately one beat length L between the symmetric and antisymmetric edge modes 1 and 2. As a result, the light focused into the left array (see the blue arrow in the upper row) is completely switched to the right array at the output. The switching curves presented as dependences of the power fractions in the left and right arrays $S_{l,r}^{out}$ on the input power U now predict a smoother increase in the power in the left array with increasing U. The experimental output intensity distributions are shown in the right column of Fig. 3, and the theoretical results are presented in the left column. With increasing pulse energy E, a monotonic increase in the energy fraction in the left array, equalization of energies in the two arrays at $E \sim 175$ nJ, and almost complete concentration of light in the left array at $E \sim 370$ nJ are observed. Finally, coupling with bulk states and radiation into the depth are observed at approximately
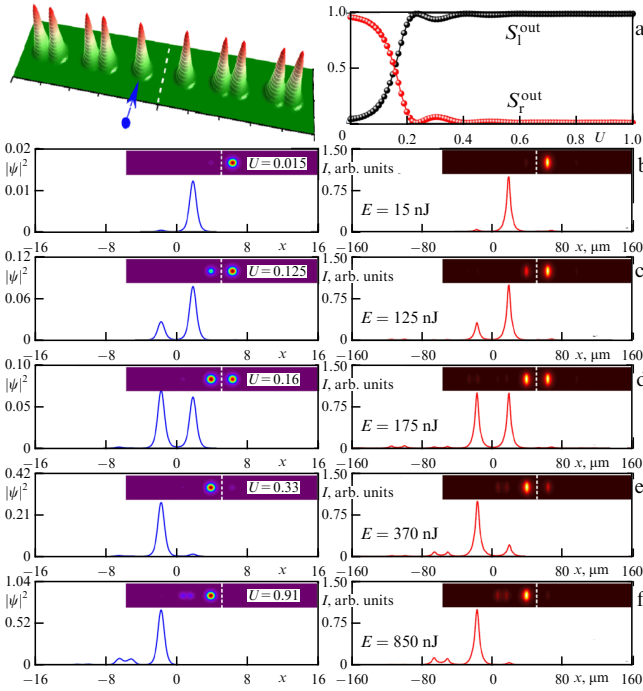
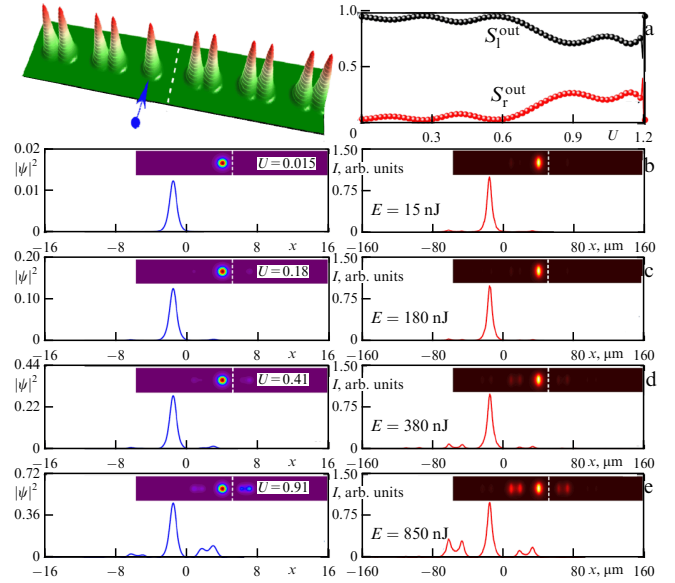**Figure 3.** Same as Fig. 2, but for a larger distance $h = 36$ μm between the two topological arrays.

Figure 4. (a) Schematic representation of interface of topological and nontopological arrays indicating excited right waveguide in the topological array and fractions of output power concentrated in left, S_l^{out}, and right, S_r^{out}, arrays as a function of input power U. (b–e) Comparison of theoretical (blue lines) and experimental (red lines) cross sections of output intensity at $y = 0$ and 2D intensity distributions (insets) for various pulse energies E. Here, $s_l = d_r = 15$ μm, $s_r = d_l = 33$ μm, $h = 31$ μm, and $p = 4.25$.

the same energy levels as for a smaller distance h. We observed stable switching in TT structures down to minimal distances $h \sim 21$ μm, at which light switches between arrays up to 3 times along the sample length, and in some energy ranges even small controlled changes in E cause rapid variations in the fractions of energy $S_{l,r}^{out}$ concentrated in two arrays. Moreover, it was demonstrated that, due to the topological protection of edge modes, the switching dynamics change only slightly with controlled introduction of disorder into this structure.

TN structures in which a topological array borders a nontopological one were also studied. The linear spectrum of modes of such a structure, shown in Fig. 1d, indicates that the dynamics of radiation propagation in it differ significantly for excitations in topological and nontopological arrays. Figure 4 shows the experimental and theoretical results obtained by focusing light into the rightmost waveguide of the topological array for a sufficiently large distance $h = 31$ μm between the two arrays. This type of excitation features a large overlap with only the localized edge mode 3 (Fig. 1h) existing in such a structure, while other modes remain virtually unexcited. As a result, with an increase in the input power, a stationary topological edge soliton branching from mode 3 is actually excited, while switching between the arrays does not occur due to the absence of interference with other modes (see the dependences $S_{l,r}^{out}$ in Fig. 4a). It is only when the pulse energy reaches sufficiently high values that a coupling with the bulk modes is observed, in both the topological and nontopological arrays, which leads to some decrease in S_l^{out} and an increase in the energy fraction in the right array. In turn, focusing light into the right, nontopological array does not lead to switching between the two parts of the structure either. Due to the absence of localized states in this part of the structure, only strong diffraction in the nontopological array is observed in the linear regime at $E \sim 15$ nJ, while, at sufficiently high energies, $E \sim 400$ nJ, the beam periodically

oscillates between two close waveguides from the nontopological part.

These results confirm the fundamental possibility of switching between topological edge states, which can be implemented in more complex geometries, including 2D structures supporting unidirectional edge modes or corner topological states. The nonlinearity of the optical medium significantly affects the switching dynamics, slowing them down and qualitatively changing the output intensity distributions, which can be especially important for designing topological switches and routers controlled by the radiation intensity.

3. Topological solitons in arrays of waveguide trimers

Su–Schrieffer–Heeger lattices with two waveguides in a unit cell, the nonlinear effects in which were considered in Section 2, represent one of the simplest implementations of a topological insulator. Increasing the number of waveguides in a unit cell in suchlike structures can significantly enrich the linear spectrum of the system, in which several topological band gaps with edge states of different symmetries can simultaneously appear [96–100]. This section is devoted to the observation of solitons bifurcating from such topological states in an array of waveguide trimers [101].

The propagation of radiation in an array consisting of waveguide trimers is described by the nonlinear Schrödinger equation (1), in which the function $\mathcal{R}(x, y) = p \sum_{m=1,3N} \mathcal{Q}(x - x_m, y)$ now specifies the profile of an array composed of Gaussian waveguides $\mathcal{Q}(x, y) = \exp[-(x^2 + y^2)/a^2]$ of width $a = 0.5$ (corresponding to 5 μm) and depth $p \approx 4.3$ (corresponding to $\delta n \sim 4.7 \times 10^{-4}$). We consider arrays consisting of $N = 5$ trimers. Micrographs of such
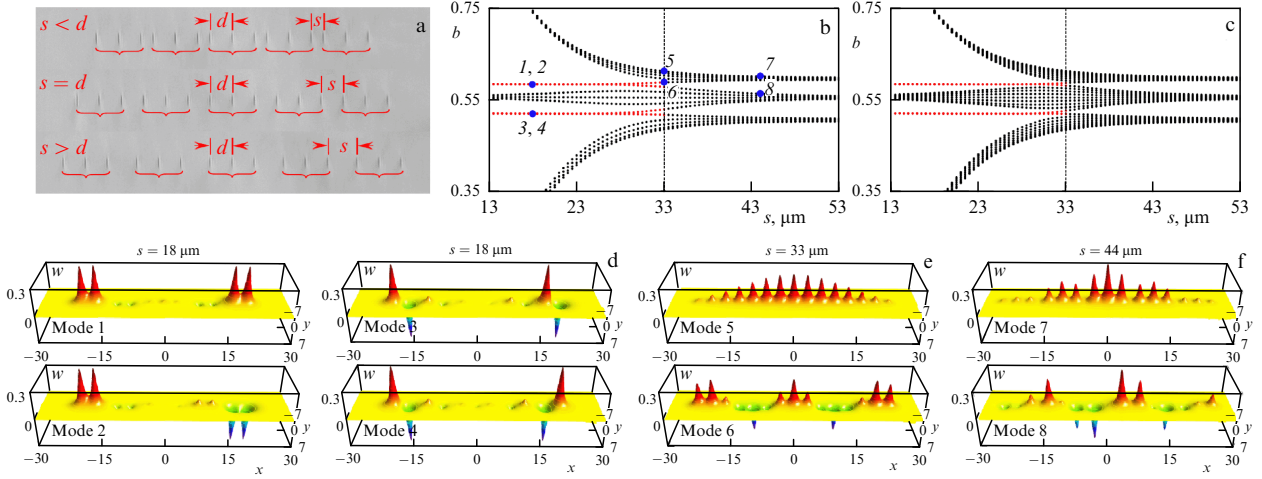
Figure 5. (a) Micrographs of waveguide trimer arrays written by laser pulses in topological and nontopological regimes. Transformation of spectrum of eigenvalues of linear modes with varying distance s in array with $N = 5$ trimers (b) and array with $N = 9$ trimers (c). Edge topological modes in spectrum correspond to red dots; bulk modes correspond to black dots. Profiles of $w(x, y)$ eigenmodes of topological (d) and nontopological (e), (f) arrays, which correspond to blue dots in Fig. b.

arrays, fabricated by the femtosecond laser writing method in fused silica, are displayed in Fig. 5a. The distance between the waveguides inside each trimer was the same, $d = 33$ μm, while the distance s between the trimers varied in a range from 18 to 44 μm, which enables implementation of either a trivial or a topological phase in this structure. The transformation of the linear spectrum of the considered array (its modes have the form $\psi(x, y, z) = w(x, y) \exp(ibz)$, where b is the propagation constant, and w is a real function describing the mode profile) with varying distance s between the trimers is illustrated in Fig. 5b for $N = 5$. At $s \geqslant d$ (the structures in the middle and bottom rows in Fig. 5a), the system is topologically trivial, since the coupling between the waveguides in neighboring trimers is weaker than that inside the trimers, and all modes are delocalized (see examples in Fig. 5e, f). In contrast, at $s < d$ (Fig. 5a, top row), the coupling between the trimers becomes stronger than that inside the trimers, which is accompanied by the appearance in the spectrum of the obtained array of two pairs of edge states, marked with red dots in Fig. 5b, in each of the two topological band gaps. Thus, the spectrum of this system is richer than that of the conventional Su–Schrieffer–Heeger structure. For a sufficiently small distance s, the pair of modes (symmetric and antisymmetric) in each band gap is virtually degenerate (cf. modes 1 and 2 or modes 3 and 4 in Fig. 5d). The topological edge states in the upper band are characterized by the presence of in-phase peaks in the two outmost waveguides (modes 1 and 2), while in the states from the lower band gap these peaks are out of phase (modes 3 and 4). The localization of topological states increases with decreasing distance s.

The appearance of edge states is consistent with the topological invariant for this structure, directly related to the Zak phase [32, 33],

$$\mathcal{W} = \frac{i}{2\pi} \int_{\mathrm{BZ}} \langle w_\kappa(x, y) | \partial_\kappa | w_\kappa(x, y) \rangle \, d\kappa \qquad (3)$$

(it is calculated for an x-periodic array, where $w_\kappa(x, y)$ is the x-periodic Bloch mode corresponding to the Bloch momentum κ, and integration is carried out over the first Brillouin zone), acquiring nonzero values 1, 2, and 1 for the upper, middle, and lower bands in the topological regime for $s < d$ and remaining equal to 0 for all bands in the trivial regime for $s \geqslant d$. The same invariant is used to describe the topological properties of conventional Su–Schrieffer–Heeger lattices. The spectrum of a larger array with $N = 9$ trimers (Fig. 5c) is virtually the same: with an increase in the number of trimers, only the density of states in the allowed bands increases. The stability of such topological states was tested by adding a small disorder to the depths and positions of the waveguides in the array, which did not lead to noticeable shifts in the propagation constants of the edge states.

Edge topological solitons bifurcate in the presence of nonlinearity from linear edge states for $s < d$. They can also be found in the form $\psi(x, y, z) = w(x, y) \exp(ibz)$ from nonlinear equation (1), where, unlike the linear problem, the propagation constant is now an independent variable determining the soliton power $U = \int |\psi|^2 \, dx \, dy$. The edge-soliton profile is determined by the symmetry of the linear edge state from which such a soliton bifurcates. Figure 6a shows a family of out-of-phase solitons arising from out-of-phase edge states in the lower topological band gap (see the first row of Fig. 6c, where typical solutions of this type are presented). Unlike ordinary surface solitons, edge solitons are formed even at low values of power U, i.e., they are objects with no threshold. When their propagation constant enters the allowed band, shown in gray in Fig. 6a, as a result of coupling with bulk modes, the soliton acquires a long tail in the depth of the array (state 2 in Fig. 6c). Interaction with bulk modes leads to the appearance of several branches of solutions, Fig. 6a only displaying the simplest of them. The branches of solutions shown in black in this figure correspond to stable solitons, and the magenta branches, to unstable ones. The stability of solitons was analyzed by adding random small noise ρ (up to 5% in amplitude) to the initial field distribution and propagating such a state $\psi|_{z=0} = w(x, y)[1 + \rho(x, y)]$ to distances $z \sim 10^4$, two orders of magnitude greater than the sample length, which allows detecting even the weakest instabilities. It is worth noting that, even when passing to the upper band gap, the out-of-phase soliton with the lowest power U (state 3 in Fig. 6a)
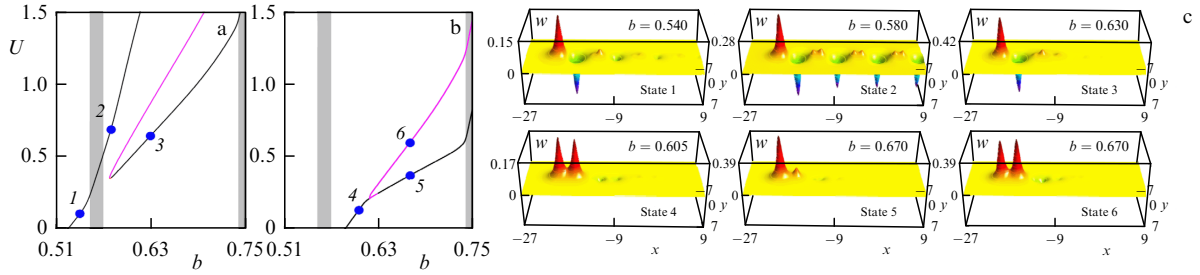
Figure 6. Families of solitons bifurcating from out-of-phase (a) and in-phase (b) linear topological states in array with $s = 18$ μm. Black branches of solutions correspond to stable states, and magenta branches correspond to unstable solitons. Areas shaded in gray correspond to allowed bands. (c) Examples of out-of-phase (upper row) and in-phase (lower row) topological solitons corresponding to blue dots in Figs a and b.

remains stable and well localized until its propagation constant reaches the boundary of the upper allowed band.

The second type of topological edge soliton with two in-phase peaks in the two outmost waveguides bifurcates from the linear edge state directly in the upper topological band gap (Fig. 6b and state 4 in Fig. 6c). The in-phase family divides into two branches with increasing b. One of them, with a lower power U, is stable and corresponds to a strongly asymmetric state, in which almost all the power is concentrated in one edge waveguide (state 5 in Fig. 6c). The other branch is characterized by virtually equal in-phase peaks in the two edge waveguides (state 6 in Fig. 6c) and is highly unstable. In the nontopological regime, at $s \geqslant d$, nonlinear states localized at the edge of the array can exist only in a semi-infinite band gap and only above a significant threshold in power U.

One of the most characteristic features of this system is that out-of-phase and in-phase edge solitons can coexist in different topological band gaps or in the same one. They feature qualitatively different phase structures and intensity distributions, which allows their selective excitation by correctly selected initial distributions. For experiments with out-of-phase solitons, we used two out-of-phase beams focused into the outermost waveguides of the structure and providing the greatest overlap with the wave field of the target state (Fig. 6c, states 1 and 3). To generate two independent beams, we used radiation from a Spitfire HP Ti:sapphire laser system (Spectra Physics) passing through a Michelson interferometer with the possibility of smooth phase tuning between the beams. To control the excitation efficiency of solitons of this type, we measured the fraction $S_2 = U_2/U$ of the total power remaining in the two outermost excited waveguides at the output of the sample (this value can be obtained by digitizing the output intensity distributions recorded with a scientific CMOS camera). Typical output intensity distributions for a nontopological array with $s = 44$ μm (Fig. 7a) reflect fairly slow diffraction at low energies, with most of it being distributed among all three channels of the outermost trimer even at the largest values of E, implying that no soliton is formed. The fraction of energy S_2 concentrated in the two outermost channels does not exceed 0.5–0.6. In a homogeneous array with $s = 33$ μm (Fig. 7b), strong diffraction into the array depth in the linear mode and gradual compression to two outermost waveguides with increasing pulse energy are observed, i.e., a soliton is formed if energy exceeds a certain threshold. It should be emphasized that, due to the pulsed nature of excitation, the tails of the spatial distributions, where the contribution from the pulse wings in the linear mode can be the strongest, are

somewhat more pronounced in the experiment than in the theoretical modeling. In a homogeneous array, S_2 increases monotonically from zero to ~ 0.7, indicating the existence of an energy threshold for soliton formation. The picture alters qualitatively in the topological mode at $s = 18$ μm (Fig. 7c), when the soliton is excited even at low energies, and most of the energy remains in the two outermost waveguides. The high excitation efficiency is confirmed by large values of $S_2 \sim 0.8$ for almost all energies (however, due to the narrowness of the allowed band between two topological band gaps, radiation into the array depth upon crossing the gap was not actually observed).

To excite in-phase edge solitons, we used the fact that, even at moderate power levels, such solitons (from the stable branch) become strongly asymmetric, and most of their power is concentrated in one outermost waveguide (Fig. 6c, state 5). In this case, single-channel excitation was used. To illustrate its efficiency for $s = 18$ μm, Fig. 8 displays the dependences of the fractions of the output power concentrated in one S_1 and two S_2 outermost waveguides. At low pulse energies, $E = 15$ nJ, almost all the power is concentrated in the outermost waveguide, while at $E \sim 235$ nJ, a significant part of it is switched to the second waveguide. This observation is consistent with the scenario of excitation of a state dynamically oscillating between two channels, since this pulse energy is still insufficient to form a stable asymmetric edge soliton. Its formation is observed for single-channel excitation at $E > 300$ nJ, and the profile of such a soliton remains virtually unaltered over a wide energy range. Note also that, with suchlike excitation and for such distances, virtually all the light remains at the output in the two outer waveguides of the array.

Thus, the diversity of topological solitons increases significantly when using arrays whose unit cells contain three or more waveguides. This feature may be especially important for the potential observation of yet undetected vortex topological solitons and for studying nonlinear interactions of topological states with various types of symmetry.

4. One- and two-dimensional topological π-solitons in dynamic Su–Schrieffer–Heeger lattices

In the previous sections, it was shown that, in static Su–Schrieffer–Heeger systems and similar structures, topological phases arise at a certain direction of shift of waveguides in unit cells. In addition to such 'static' systems, there is also a whole class of 'dynamic' topological systems or Floquet
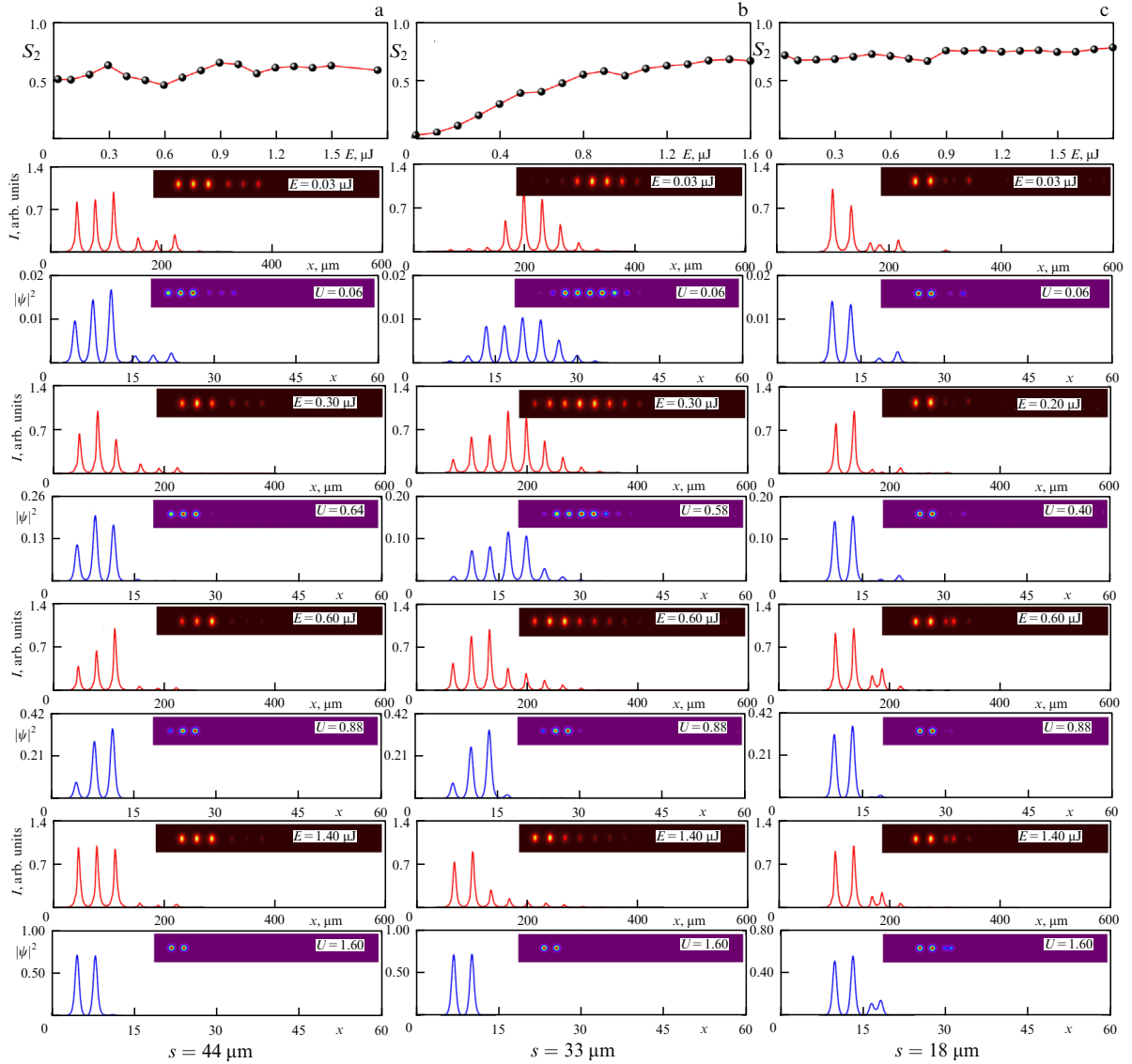
Figure 7. Nonlinear localization and formation of solitons in nontopological arrays (with $s = 44$ μm (a) and $s = 33$ μm (b)) and a topological array ($s = 18$ μm (c)) upon excitation of two outermost waveguides by antiphase beams. Upper row of each column shows experimentally measured fraction of energy S_2 concentrated in the two leftmost waveguides at the output as a function of input pulse energy E. Each column presents a comparison of experimental (red lines) and theoretical (blue lines) cross sections of output intensity at $y = 0$ and 2D intensity distributions (insets) for increasing input energy E.

systems, where such phases appear only due to periodic modulations of the structure along the evolutionary coordinate, for example, time in atomic systems or the propagation coordinate in waveguide structures. In such dynamical systems, the evolution is characterized by quasi-propagation constants (or quasi-energies) which replace the usual propagation constants in static arrays and are now also periodic quantities with a period of $2\pi/Z$ due to the longitudinal Z periodicity of the system. Edge states in the spectrum of such systems can appear at the points where the allowed band overlaps with its own Floquet replicas arising due to the periodicity of the quasi-propagation constant. Therefore, they are usually called π-modes, since in discrete models their quasi-propagation constants turn out to be $b = \pm\pi/Z$, while edge states in static, discrete lattices having the Su–Schrieffer–Heeger form appear at $b = 0$. In this section, we describe π-solitons bifurcating from such π-modes in dynamic Su–Schrieffer–Heeger lattices in the presence of nonlinearity in the medium [136].

To describe the features of the formation of such states, we consider a shallow array of waveguides in which the centers of the waveguides periodically oscillate along certain trajectories in the direction of radiation propagation. The dynamics of radiation propagation in this structure are described by the following equation for the amplitude of the light field ψ:

$$i\frac{\partial\psi}{\partial z} = -\frac{1}{2}\left(\frac{\partial^2}{\partial x^2} + \frac{\partial^2}{\partial y^2}\right)\psi - \mathcal{R}(x,y,z)\psi - |\psi|^2\psi, \quad (4)$$

where, in contrast to Eqn (1), the optical potential $\mathcal{R}$ also depends on the propagation coordinate z. In the 1D case, we consider a Su–Schrieffer–Heeger array with $N = 7$ dimers, the refractive index of which is described by the function $\mathcal{R} = p\sum_{m=1,N}[\exp(-x_{1m}^2/a_x^2 - y^2/a_y^2) + \exp(-x_{2m}^2/a_x^2 - y^2/a_y^2)]$, where $x_{1m} = x_m + d/2 + r\cos(\omega z)$ and $x_{2m} = x_m - d/2 - r\cos(\omega z)$ are the coordinates of the waveguide centers in each unit cell containing two waveguides; $\omega = 2\pi/Z$ is the
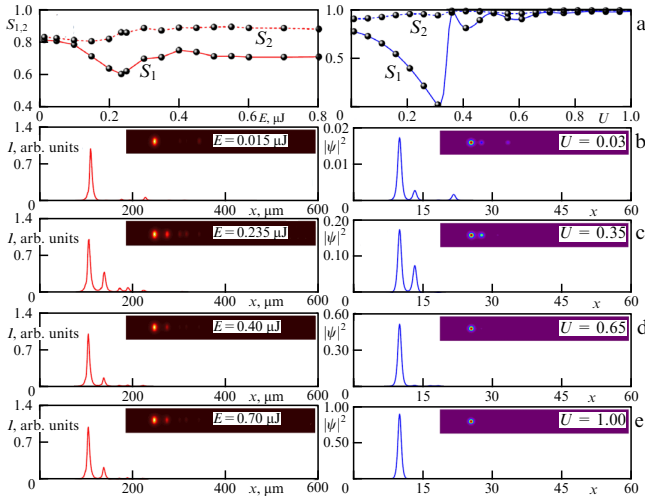
Figure 8. Formation of an in-phase edge soliton in a topological array with $s = 18$ μm with single-channel excitation (left column — experiment, right column — numerical simulation). (a) Fraction of output power concentrated in the leftmost (S_1) or in the two leftmost channels (S_2) as a function of input pulse energy E (in the experiment) or power U (in the spatial numerical simulation). (b–e) One-dimensional and two-dimensional output intensity distributions for various input energies.

oscillation frequency of the waveguide centers; Z is the longitudinal period; $x_m = x - 2md$; r is the waveguide amplitude, which usually varies in experiments from 1 to 11 μm; $d = 3$ corresponds to a distance between the waveguides of 30 μm at $r = 0$ (the width of the unit cell is $2d$); $a_x = 0.25$ (2.5 μm), and $a_y = 0.75$ (7.5 μm) are the widths of the waveguides, elliptical due to the technology of their writing; and $p \approx 4.5$ is the normalized modulation depth of the refractive index in the array. Such an array is schematically displayed in Fig. 9a. The distance between the waveguides in each unit cell of such a structure $d - 2r\cos(\omega z)$ varies periodically with the distance z, transforming this system from the instantaneous topological phase (in which the coupling between the waveguides in adjacent dimers is stronger than the coupling in dimers) to the instantaneous nontopological phase (where the coupling between the dimers is weaker than the coupling in dimers), with the average distance between the waveguides being d. Micrographs of such 1D arrays, fabricated by the femtosecond laser writing method in fused silica, are shown in Fig. 9b at various distances z. The array period $Z = 33$ mm was chosen in such a way that exactly three periods of this Floquet structure fit into the sample length.

Nontrivial topological properties in this system arise from longitudinal variations in the structure (waveguide oscillations). Its linear eigenmodes are the Floquet modes $\psi = w(x, y, z)\exp(ibz)$, where b is the propagation quasi-constant (in the first Brillouin zone $b \in [-\omega/2, +\omega/2)$), and $w(x, y, z) = w(x, y, z + Z)$ is a periodic complex function satisfying the equation

$$bw = \frac{1}{2}\left(\frac{\partial^2}{\partial x^2} + \frac{\partial^2}{\partial y^2}\right)w + \mathcal{R}w + i\frac{\partial w}{\partial z} + |w|^2 w \qquad (5)$$

(for the sake of illustration, we retain in it the nonlinear term, which is omitted when calculating the linear spectrum, since the same equation is used to calculate the profiles of π-solitons). The transformation of the linear spectrum with increasing

amplitude of the waveguide oscillations r is shown in Fig. 9c. In the Floquet system, the propagation quasi-constant is defined by $\text{mod}(\omega)$, and in Fig. 9c we show the spectrum within three longitudinal Brillouin zones. The gray lines correspond to delocalized bulk modes, and the red ones, to edge topological modes. They arise from the overlap points of Floquet replicas of the same band, since the longitudinal modulation of the refractive index leads to hybridization of states at the band edges, removing their degeneracy and leading to the opening of the band gap. Since the array considered here is symmetric, localized states appear simultaneously at both of its boundaries. The quasi-propagation constants of such π-modes fall into the band gap, which guarantees the absence of coupling with the bulk modes. Their localization is enhanced with increasing band gap width (cf. Figs 9d and 9e), which, however, is a nonmonotonic function of the oscillation amplitude r. The π-modes oscillate in the period Z, but exactly reproduce their profile after each period of the structure. It is noteworthy that the main intensity maximum in such states is not always concentrated in the outermost waveguide: for example, in Fig. 9e, it is seen that, at $z = Z/2$, when the lattice is in the nontopological phase, the intensity maximum switches to the second waveguide. Less localized π-modes at smaller r values undergo even more significant profile transformations over one Z-period (Fig. 9d). The topological properties of this system are characterized by the so-called π-invariant w_π for the band gap. Details of its calculation are reported in [124, 128]. In the topological phase at $r \neq 0$, this invariant takes an integer value $w_\pi = 1$, indicating the appearance of edge states.

When nonlinearity is taken into account, edge π-solitons can be formed in the oscillating array. Their profiles can be obtained using an iterative procedure enabling calculation of the field distribution $w(x, y, z)$ over one Z-period, the quasi-propagation constant b, and the averaged soliton amplitude $A = Z^{-1}\int_z^{z+Z}\max|\psi|\,dz$, which are determined by the soliton power $U = \int\int|\psi|^2\,dx\,dy$ (Fig. 10). π-solitons bifurcate from the linear π-mode; their amplitude increases with increasing power (Fig. 10b), and the quasi-propagation constant gradually shifts toward the band gap boundary (Fig. 10a). This is accompanied by a change in the degree of spatial localization of the soliton, similar to what occurs for edge solitons in static waveguide systems. Periodic oscillations of the π-soliton profile are shown in Fig. 10c. Such states are quite stable, which is confirmed by analyzing their propagation with noise, and they do not really lose power due to radiation up to the waveguide oscillation amplitudes $r = 9$ μm. Due to this, they can be observed even after hundreds of Z-periods of the structure. Stability analysis showed that, at $r > 5$ μm, 1D π-solitons are stable as long as their quasi-propagation constant remains in the band gap, but they lose stability in the band as a result of coupling with bulk modes.

For the experimental observation of 1D π-solitons in a fused silica sample, a set of arrays with a waveguide oscillation amplitude gradually increasing from $r = 1$ to 11 μm was made (see the micrographs in Fig. 9b). In addition, to written the dynamics at the internal points of the period, in addition to the structures containing three full periods, arrays of fractional length, $2.25Z$, $2.50Z$, and $2.75Z$, were written. The leftmost waveguide of the array was excited in the experiments. Figure 11 shows the cross sections at $y = 0$ and the complete 2D intensity distributions at two different distances $z = 2.50Z$ and $z = 3.00Z$ at different pulse energies
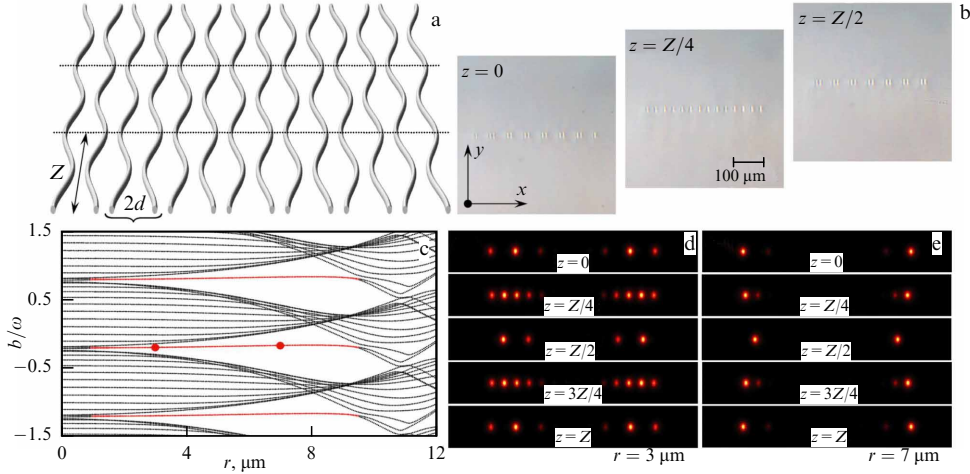
Figure 9. (a) Schematic representation of a 1D oscillating waveguide array containing 7 unit cells, (b) Micrographs of a waveguide array fabricated by femtosecond laser writing method at various distances in topological phase ($z = 0$), locally homogeneous array ($z = Z/4$), and nontopological phase ($z = Z/2$). (c) Quasi-propagation constants of Floquet modes of an oscillating waveguide array as a function of amplitude r of waveguide oscillations. Three longitudinal Brillouin zones are shown. (d, e) Intensity distributions at various distances within one period Z in linear π-modes for two different oscillation amplitudes r corresponding to red circles in panel c. In all cases, $Z = 33$ mm.
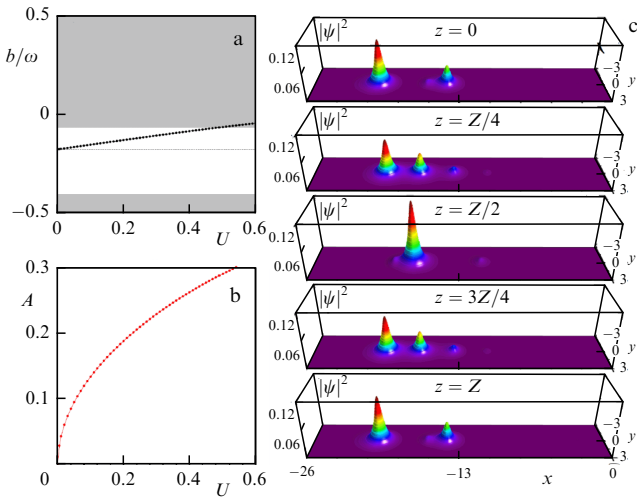

Figure 10. (a) Quasi-propagation constant b and (b) averaged amplitude A of a soliton as functions of its power U. Gray area in panel a corresponds to allowed band, while white area corresponds to band gap. Horizontal line indicates quasi-propagation constant of linear π-mode. (c) Intensity distributions in a π-soliton with power $U = 0.5$ for various distances within one longitudinal period of the array. Here, $r = 6$ μm, $Z = 33$ mm.

Figure 11. Sections at $y = 0$ of intensity distributions and full 2D intensity distributions (insets) at two different distances z and at different pulse energies E illustrating formation of 1D π-solitons. Insets with dark brown background display results of numerical simulation. Here, $r = 9$ μm and $Z = 33$ mm.

generated by a Ti:sapphire laser system. The localization at the boundary of the oscillating array is enhanced rapidly with increasing r, and, already at $r \geqslant 7$ μm, the edge states are efficiently excited even when light is fed into one waveguide. At $r = 9$ μm, the light at certain distances z is localized virtually in one channel (Fig. 11), and it is clear that, for example, at $z = 2.50Z$, the light is switched to the waveguide adjacent to the outermost waveguide, and at $z = 2.25Z$, the power is divided virtually equally between the two outermost waveguides. At $r = 9$ μm, well-localized periodically oscillating states are observed for pulse energies up to $E = 900$ nJ (rows 1–3 in Fig. 11), and only at $E \sim 1000$ nJ radiation into the array depth become noticeable due to the coupling with bulk modes (row 4). For smaller values of the oscillation amplitude r, the energy range in which stably oscillating nonlinear states are formed is reduced, since the band gap
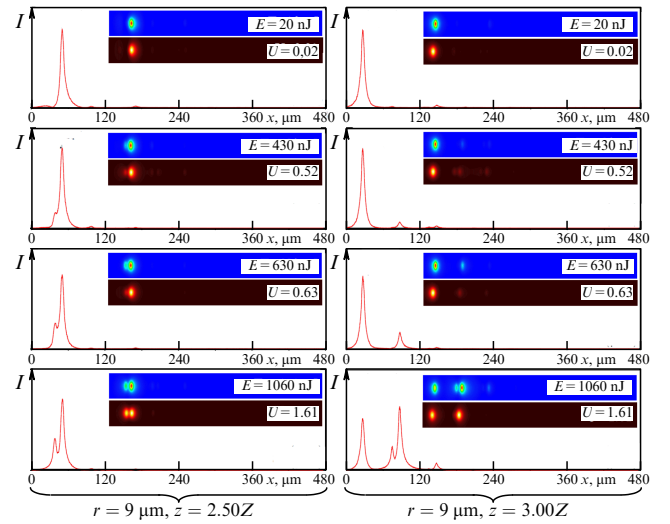
width decreases with decreasing r. It should be noted that, at the same pulse energies, excitation of the waveguide in the bulk of the array does not lead to the formation of localized states.

To observe 2D π-solitons, we used a version of the Su–Schrieffer–Heeger lattice, each unit cell (quadrimer) of which contains four waveguides. Their centers periodically oscillate along the unit cell diagonals. The refractive index in such a 2D Floquet structure is described by the function

$$\mathcal{R}(x, y) = p \sum_{m,n} \left[\exp\left(-\frac{x_{1m}^2}{a_x^2} - \frac{y_{1n}^2}{a_y^2}\right) + \exp\left(-\frac{x_{2m}^2}{a_x^2} - \frac{y_{1n}^2}{a_y^2}\right) \right.$$
$$\left. + \exp\left(-\frac{x_{1m}^2}{a_x^2} - \frac{y_{2n}^2}{a_y^2}\right) + \exp\left(-\frac{x_{2m}^2}{a_x^2} - \frac{y_{2n}^2}{a_y^2}\right) \right], \quad (6)$$
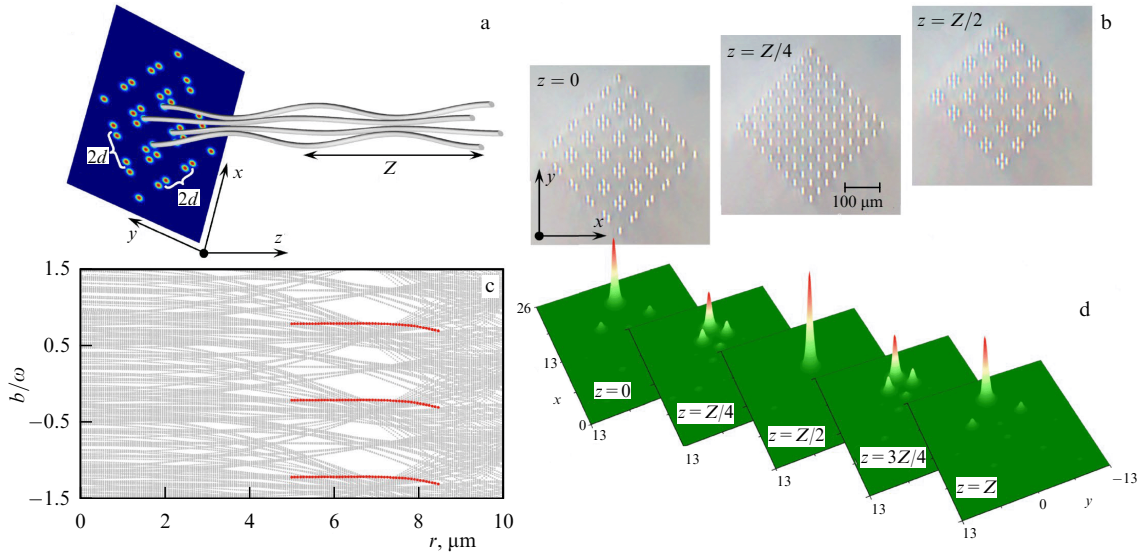
Figure 12. (a) Schematic representation of a 2D array of oscillating waveguides (for illustrative purposes, a structure with 3×3 cells is shown). (b) Micrographs of an array with 5×5 cells, fabricated by femtosecond laser-writing method, at various distances z. (c) Linear spectrum of a 2D Floquet array depending on amplitude of waveguide oscillations r (three longitudinal Brillouin zones are shown). (d) Intensity distributions in a linear 2D corner π-mode at various distances z at $r = 6$ μm. Longitudinal period of the structure $Z = 49.5$ mm.

where $x_{1m, 2m} = x_m \pm d/2 \pm r \cos(\omega z)$, $y_{1n, 2n} = y_n \pm d/2 \pm r \cos(\omega z)$ are coordinates of the centers of the four waveguides in the unit cell, $x_m = x - 2md$ and $y_n = y - 2nd$, m, n are integers, and the parameter r, as before, describes the oscillation amplitude. The oscillation period in the 2D structure was $Z = 49.5$ mm, i.e., two full periods fit into the sample length. To achieve a virtually isotropic coupling between the waveguides, their long axes were oriented along one of the diagonals of the array, and the distance between the waveguides was increased to $d = 32$ μm (see the schematic representation of the array in Fig. 12a and the micrographs of the recorded structures with 5×5 elementary cells in Fig. 12b). In fact, such an array is a higher-order Floquet insulator, periodically switching between 'instantaneous' topological and nontopological phases.

The linear spectrum of the 2D array, presented in Fig. 12c, shows that corner π-modes (red lines) can be formed; however, compared to the 1D array, these modes appear in a fairly narrow range of waveguide oscillation amplitudes. This is a consequence of the significantly more complex structure of the spectrum of static 2D Su–Schrieffer–Heeger structures, which are characterized by the presence of four allowed bands in the topological phase (in contrast to the two allowed bands observed in the spectrum of 1D topological Su–Schrieffer–Heeger lattices). In the Z-periodic Floquet array, such bands can 'fold' and overlap due to the longitudinal modulation of the refractive index (due to the finite width of the longitudinal Brillouin zone, equal to $2\pi/Z$), which yields a very complex Floquet spectrum. In the 2D case, quasi-propagation constants of corner modes can overlap with the allowed band, as in static topological insulators of higher order. An example of a linear corner mode periodically reproducing its profile in a dynamically modulated 2D array is shown in Fig. 12d. In the nonlinear regime, corner π-solitons bifurcate from such modes; for the selected oscillation amplitude $r = 7$ μm, they exist virtually in the entire band gap, since the quasi-propagation constant of the linear mode for these parameters is located at the lower edge of the band gap and increases with increasing soliton

power U. The properties of such solitons are qualitatively similar to those of the 1D solitons displayed in Fig. 10. Despite the significant oscillations that 2D solitons undergo during one longitudinal period Z, they nevertheless turn out to be dynamically stable in a cubic nonlinear medium, due to which they can be observed experimentally.

To do so, arrays with various oscillation amplitudes of waveguides ranging from $r = 1$ to 9 μm were made using the femtosecond laser writing method (see micrographs of typical arrays in Fig. 12b). The solitons were excited using a beam focused into a corner waveguide of the array (for example, in the right corner).

Figure 13 shows a comparison of the experimentally recorded and theoretically calculated output intensity distributions for single-channel excitation in the right corner for various amplitudes of waveguide oscillation in the structure. At small oscillation amplitudes $r \sim 3$ μm, when linear π-modes are absent in the Floquet spectrum, strong diffraction into the array depth is observed at all pulse energies, i.e., in this case, the nonlinearity is insufficient for forming a corner soliton at the available energy levels (Fig. 13a). A tendency towards gradual contraction of the output intensity distribution to the corner channel with increasing E is noticeable. Efficient excitation of corner π-modes occurs at oscillation amplitudes $r \geqslant 5$ μm, in which case, with increasing pulse energy E, the formation of π-solitons is observed, the range of their existence in energy E increasing with increasing waveguide oscillation amplitude r. With a further increase in the pulse energy outside this range, the corner states are delocalized due to the penetration of their quasi-propagation constant into the allowed band, leading to a coupling with bulk modes. For example, at $r = 5$ μm, well-localized corner π-solitons are formed at pulse energies $E < 300$ nJ, while already at $E \sim 400$ nJ (Fig. 13b) a migration of radiation into the array depth is observed. At $r = 7$ μm, soliton formation is observed even at pulse energies $E \sim 600$ nJ with a tendency to an insignificant increase in secondary intensity maxima in the soliton (Fig. 13c). Excitation in other corners of the lattice (for example, in the upper
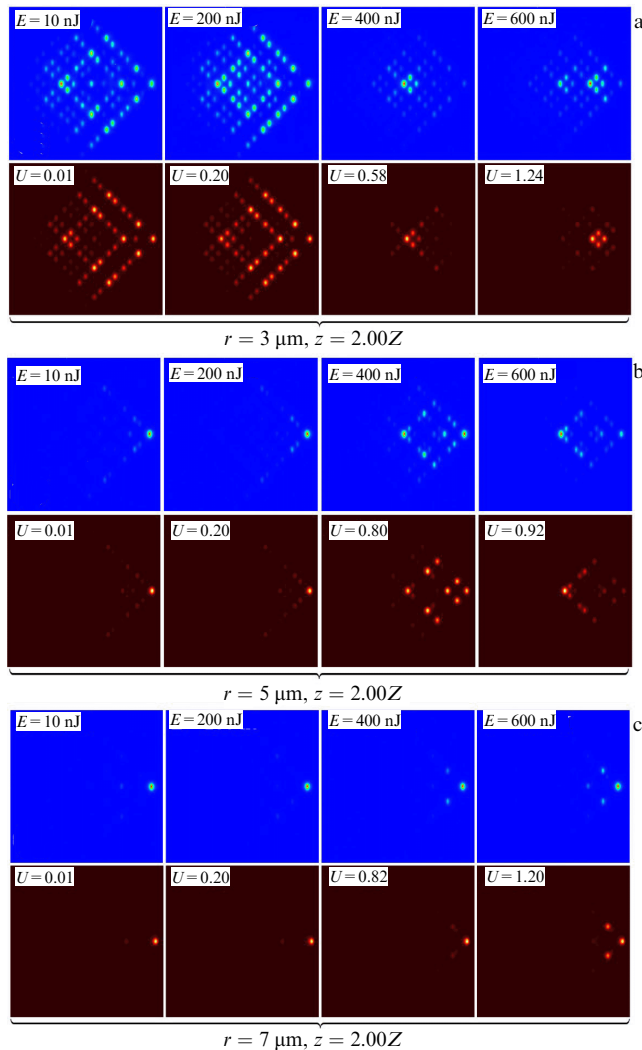
Figure 13. Excitation of 2D π-solitons in an array of oscillating waveguides. Output intensity distributions at distance $z = 2Z$ are shown for three different waveguide oscillation amplitudes. Top row in each case shows experimental intensity distributions for various pulse energies E, while bottom row presents results of theoretical modeling for various input powers U.

one) yields similar results, confirming the formation of π-solitons, while excitation in the array depth is diffracted in the specified range of pulse energies.

The above results clearly indicate that Floquet states exist in dynamically modulated waveguide systems and exhibit rich dynamics even in nonlinear propagation regimes. The nontrivial interaction of nonlinearity and topology in these structures can be used to realize soliton states with new types of symmetry that do not exist in static arrays and to observe nonlinear effects in anomalous topological Floquet systems.

5. Conclusions

The results presented demonstrate that even the simplest topological systems based on Su–Schrieffer–Heeger lattices allow observing unique interactions between nonlinear and topological effects. Stable edge solitons arising in such structures are one of the manifestations of the above-mentioned interactions. In topological systems, such phenomena as the generation of new harmonics, switching between localized states, and controlled mode transforma-

tions often acquire new, completely unexpected features. Their efficiency can be significantly enhanced due to the nontrivial topology of the system, leading to strong localization of topological states. The study of the above phenomena in topological structures of new types and with various types of nonlinearity is one of the tasks of modern, rapidly developing, nonlinear topological photonics. At present, nonlinear dissipative topological systems are of particular interest in this area. For example, topological lasers of various types (with unidirectional edge states or higher order) can be constructed based on such systems; their generation is significantly more efficient than that of conventional laser systems and, moreover, insensitive to the presence of disorder in the structure. Nonlinear effects in a completely new class of topological insulators on aperiodic lattices with new types of symmetry incompatible with crystal symmetries remain virtually unexplored. Studies in this area will potentially enable development of new types of optically controlled topological devices for protected data and information transmission.

References

1. Volkov B A, Pankratov O A *JETP Lett.* **42** 178 (1985); *Pis'ma Zh. Eksp. Teor. Fiz.* **42** 145 (1985)
2. Pankratov O A *Phys. Usp.* **61** 1116 (2018); *Usp. Fiz. Nauk* **188** 1226 (2018)
3. Vedeneev S I *Phys. Usp.* **60** 385 (2017); *Usp. Fiz. Nauk* **187** 411 (2017)
4. Tarasenko S A *Phys. Usp.* **61** 1026 (2018); *Usp. Fiz. Nauk* **188** 1129 (2018)
5. Hasan M Z, Kane C L *Rev. Mod. Phys.* **82** 3045 (2010)
6. Qi X-L, Zhang S-C *Rev. Mod. Phys.* **83** 1057 (2011)
7. Süsstrunk R, Huber S D *Science* **349** 47 (2015)
8. Huber S D *Nature Phys.* **12** 621 (2016)
9. Peng Y-G et al. *Nat. Commun.* **7** 13368 (2016)
10. He C et al. *Nature Phys.* **12** 1124 (2016)
11. Lu J et al. *Nature Phys.* **13** 369 (2017)
12. Jotzu G et al. *Nature* **515** 237 (2014)
13. Goldman N et al. *Proc. Natl. Acad. Sci. USA* **110** 6736 (2013)
14. Leder M et al. *Nat. Commun.* **7** 13112 (2016)
15. Zhang W et al. *Phys. Rev. Lett.* **123** 254103 (2019)
16. Zhai H et al. *New J. Phys.* **18** 080201 (2016)
17. Nalitov A V, Solnyshkov D D, Malpuech G *Phys. Rev. Lett.* **114** 116401 (2015)
18. Bardyn C-E et al. *Phys. Rev. B* **91** 161413 (2015)
19. Karzig T et al. *Phys. Rev. X* **5** 031001 (2015)
20. Kartashov Ya V, Skryabin D V *Optica* **3** 1228 (2016)
21. Bleu O, Solnyshkov D D, Malpuech G *Phys. Rev. B* **93** 085438 (2016)
22. St-Jean P et al. *Nat. Photon.* **11** 651 (2017)
23. Klembt S et al. *Nature* **562** 552 (2018)
24. Su R et al. *Sci. Adv.* **7** eabf8049 (2021)
25. Wang Z et al. *Nature* **461** 772 (2009)
26. Hafezi M et al. *Nature Phys.* **7** 907 (2011)
27. Khanikaev A B et al. *Nature Mater.* **12** 233 (2013)
28. Rechtsman M C et al. *Nature* **496** 196 (2013)
29. Maczewsky L J et al. *Nat. Commun.* **8** 13756 (2017)
30. Mukherjee S et al. *Nat. Commun.* **8** 13918 (2017)
31. Klimov V V et al. *Phys. Rev. B* **98** 075433 (2018)
32. Lu L, Joannopoulos J D, Soljačić M *Nat. Photon.* **8** 821 (2014)
33. Ozawa T et al. *Rev. Mod. Phys.* **91** 015006 (2019)
34. Kim M, Jacob Z, Rho J *Light Sci. Appl.* **9** 130 (2020)

35. Xie B et al. *Nat. Rev. Phys.* **3** 520 (2021)
36. Lindner N H, Refael G, Galitski V *Nature Phys.* **7** 490 (2011)
37. Rudner M S et al. *Phys. Rev. X* **3** 031005 (2013)
38. Rudner M S, Lindner N H *Nat. Rev. Phys.* **2** 229 (2020)
39. Noh J et al. *Phys. Rev. Lett.* **120** 063902 (2018)
40. Dong J-W et al. *Nature Mater.* **16** 298 (2017)
41. Wu X et al. *Nat. Commun.* **8** 1304 (2017)
42. Gao F et al. *Nature Phys.* **14** 140 (2018)
43. He X-T et al. *Nat. Commun.* **10** 872 (2019)
44. Peterson C W et al. *Nature* **555** 346 (2018)
45. Noh J et al *Nat. Photon.* **12** 408 (2018)
46. Mittal S et al. *Nat. Photon.* **13** 692 (2019)
47. El Hassan A et al. *Nat. Photon.* **13** 697 (2019)
48. Smirnova D et al. *Appl. Phys. Rev.* **7** 021306 (2020)
49. Rachel S *Rep. Prog. Phys.* **81** 116501 (2018)
50. Szameit A, Rechtsman M C *Nature Phys.* **20** 905 (2024)
51. Dobrykh D A et al. *Phys. Rev. Lett.* **121** 163901 (2018)
52. Lan Z, You J W, Panoiu N C *Phys. Rev. B* **101** 155422 (2020)
53. Ivanov S K et al. *Laser Photon. Rev.* **16** 2100398 (2022)
54. Kruk S S et al. *Nano Lett.* **21** 4592 (2021)
55. Hadad Y et al. *Nat. Electron.* **1** 178 (2018)
56. Hadad Y, Khanikaev A B, Alù A *Phys. Rev. B* **93** 155112 (2016)
57. Maczewsky L J et al. *Science* **370** 701 (2020)
58. Zangeneh-Nejad F, Fleury R *Phys. Rev. Lett.* **123** 053902 (2019)
59. Banerjee R, Mandal S, Liew T C H *Phys. Rev. Lett.* **124** 063901 (2020)
60. Leykam D, Chong Y D *Phys. Rev. Lett.* **117** 143901 (2016)
61. Lumer Y et al. *Phys. Rev. A* **94** 021801 (2016)
62. Lumer Y et al. *Phys. Rev. Lett.* **111** 243905 (2013)
63. Mukherjee S, Rechtsman M C *Science* **368** 856 (2020)
64. Ablowitz M J, Curtis C W, Ma Y-P *Phys. Rev. A* **90** 023813 (2014)
65. Ablowitz M J, Cole J T *Phys. Rev. A* **96** 043868 (2017)
66. Ablowitz M J, Cole J T *Phys. Rev. A* **99** 033821 (2019)
67. Zhang Z et al. *Nat. Commun.* **11** 1902 (2020)
68. Ivanov S K et al. *ACS Photon.* **7** 735 (2020)
69. Ivanov S K et al. *Opt. Lett.* **45** 1459 (2020)
70. Ivanov S K et al. *Phys. Rev. A* **103** 053507 (2021)
71. Mukherjee S, Rechtsman M C *Phys. Rev. X* **11** 041057 (2021)
72. Mukherjee S, Rechtsman M C *Optica* **10** 1310 (2023)
73. Zhong H et al. *Adv. Photon.* **3** (5) 056001 (2021)
74. Smirnova D A et al. *Phys. Rev. Research* **3** 043027 (2021)
75. Ren B et al. *Nanophotonics* **10** 3559 (2021)
76. Kirsch M S et al. *Nature Phys.* **17** 995 (2021)
77. Hu Z et al. *Light Sci. Appl.* **10** 164 (2021)
78. Ren B et al. *Light Sci. Appl.* **12** 194 (2023)
79. López Carreño J C, Bermúdez Feijoo S, Stobińska M *npj Nanophoton.* **1** 3 (2024)
80. Volovik G E *JETP Lett.* **53** 222 (1991); *Pis'ma Zh. Eksp. Teor. Fiz.* **53** 208 (1991)
81. Gurarie V *Phys. Rev. B* **83** 085426 (2011)
82. Manmana S R et al. *Phys. Rev. B* **86** 205119 (2012)
83. Su W P, Schrieffer J R, Heeger A J *Phys. Rev. Lett.* **42** 1698 (1979)
84. Solnyshkov D D et al. *Phys. Rev. Lett.* **118** 023901 (2017)
85. Gorlach M A, Slobozhanyuk A P *Nanosystems Phys. Chem. Math.* **8** 695 (2017)
86. Chaunsali R et al. *Phys. Rev. B* **103** 024106 (2021)
87. Zykin A Y, Skryabin D V, Kartashov Y V *Opt. Lett.* **46** 2123 (2021)
88. Bongiovanni D et al. *Phys. Rev. Lett.* **127** 184101 (2021)
89. Hang C et al. *Phys. Rev. A* **103** L040202 (2021)
90. Malkova N et al. *Opt. Lett.* **34** 1633 (2009)
91. Xia S et al. *Light Sci. Appl.* **9** 147 (2020)
92. Guo M et al. *Opt. Lett.* **45** 6466 (2020)
93. Bisianov A et al. *Phys. Rev. A* **100** 063830 (2019)
94. Pieczarka M et al. *Optica* **8** 1084 (2021)
95. Pernet N et al. *Nature Phys.* **18** 678 (2022)
96. Jin L *Phys. Rev. A* **96** 032103 (2017)
97. Midya B, Feng L *Phys. Rev. A* **98** 043838 (2018)
98. Martinez Alvarez V M, Coutinho-Filho M D *Phys. Rev. A* **99** 013833 (2019)
99. Wang Y et al. *Phys. Rev. B* **103** 014110 (2021)
100. Zhang Y et al. *Opt. Express* **29** 42827 (2021)
101. Kartashov Y V et al. *Phys. Rev. Lett.* **128** 093901 (2022)
102. Kartashov Y V, Konotop V V *Chaos Solitons Fractals* **179** 114461 (2024)
103. Ma J, Xi X, Sun X *Laser Photon. Rev.* **13** 1900087 (2019)
104. Merlo J M et al. *J. Opt.* **23** 065001 (2021)
105. Chen Q et al. *ACS Photon.* **8** 1400 (2021)
106. Kraus Y E et al. *Phys. Rev. Lett.* **109** 106402 (2012)
107. Zilberberg O et al. *Nature* **553** 59 (2018)
108. Krueckl V, Richter K *Phys. Rev. B* **85** 115433 (2012)
109. Li C et al. *Phys. Rev. A* **99** 053814 (2019)
110. Zhang Y et al. *Laser Photon. Rev.* **12** 1700348 (2018)
111. Zhong H et al. *Opt. Lett.* **44** 3342 (2019)
112. Ma X et al. *Opt. Lett.* **45** 5311 (2020)
113. Kartashov Y V, Skryabin D V *Phys. Rev. Lett.* **119** 253904 (2017)
114. Bazhan N, Malomed B, Yakimenko A *Opt. Lett.* **46** 6067 (2021)
115. Efremidis N K *Phys. Rev. A* **104** 053531 (2021)
116. Song W et al. *Laser Photon. Rev.* **14** 1900193 (2020)
117. Arkhipova A A et al. *Nanophotonics* **11** 3653 (2022)
118. Garanovich I L et al. *Phys. Rep.* **518** 1 (2012)
119. Kitagawa T et al. *Phys. Rev. B* **82** 235114 (2010)
120. Rudner M S et al., arXiv:1212.3324
121. Rudner M S, Lindner N H *Nat. Rev. Phys.* **2** 229 (2020)
122. Asbóth J K, Tarasinski B, Delplace P *Phys. Rev. B* **90** 125143 (2014)
123. Dal Lago V, Atala M, Foa Torres L E F *Phys. Rev. A* **92** 023624 (2015)
124. Fruchart M *Phys. Rev. B* **93** 115429 (2016)
125. Zhang Y et al. *ACS Photon.* **4** 2250 (2017)
126. Petráček J, Kuzmiak V *Phys. Rev. A* **101** 033805 (2020)
127. Mandal S, Kar S *Phys. Rev. B* **109** 195124 (2024)
128. Cheng Q et al. *Phys. Rev. Lett.* **122** 173901 (2019)
129. Wu S et al. *Phys. Rev. Research* **3** 023211 (2021)
130. Song W et al. *Laser Photon. Rev.* **15** 2000584 (2021)
131. Sidorenko A et al. *Phys. Rev. Research* **4** 033184 (2022)
132. Cheng Z et al. *Phys. Rev. Lett.* **129** 254301 (2022)
133. Zhu W et al. *Nat. Commun.* **13** 11 (2022)
134. Zhong H et al. *Phys. Rev. A* **107** L021502 (2023)
135. Ivanov S K, Kartashov Y V *Chaos Solitons Fractals* **174** 113866 (2023)
136. Arkhipova A A et al. *Sci. Bull.* **68** 2017 (2023)
137. Jensen S *IEEE J. Quantum Electron.* **18** 1580 (1982)
138. Nguyen V H et al. *Opt. Lett.* **45** 5221 (2020)